

Article

Not peer-reviewed version

---

# Investigation on the Coordination Bonding Nature of Actinide-Doped Endohedral Borospherenes $An@B_4O_0/+/-$ ( $An = U, Np, Pu, Am, Cm$ )

---

[Xiao-Ni Zhao](#), Zhi-Hong Wei, [Si-Dian Li](#)\*

Posted Date: 30 October 2024

doi: 10.20944/preprints202410.2373.v1

Keywords: Actinides; Metallo-Borospherenes; First-Principles Theory; Structures; Coordination Bonding Patterns



Preprints.org is a free multidisciplinary platform providing preprint service that is dedicated to making early versions of research outputs permanently available and citable. Preprints posted at Preprints.org appear in Web of Science, Crossref, Google Scholar, Scilit, Europe PMC.

Copyright: This open access article is published under a Creative Commons CC BY 4.0 license, which permit the free download, distribution, and reuse, provided that the author and preprint are cited in any reuse.

Disclaimer/Publisher's Note: The statements, opinions, and data contained in all publications are solely those of the individual author(s) and contributor(s) and not of MDPI and/or the editor(s). MDPI and/or the editor(s) disclaim responsibility for any injury to people or property resulting from any ideas, methods, instructions, or products referred to in the content.

## Article

# Investigation on the Coordination Bonding Nature of Actinide-Doped Endohedral Borospherenes $An@B_{40}^{0/+/-}$ ( $An = U, Np, Pu, Am, Cm$ )

Xiao-Ni Zhao, Zhi-Hong Wei and Si-Dian Li \*

Institute of Molecular Science, Key Laboratory of Chemical Biology and Molecular Engineering of Education Ministry, Shanxi University, Taiyuan 030006, China; lisidian@sxu.edu.cn

**Abstract:** Endohedral metallo-borospherenes  $M@B_{40}$  have received considerable attention since the discovery of  $B_{40}$  in 2014. However, the coordination bonding nature of most of the actinide-doped endohedral  $An@B_{40}$  still remains in disputes or unexplored. Extensive first-principles theory calculations performed herein unveil the ground states of triplet  $U@B_{40}$  (**1**,  $C_{2v}$ ,  $^3A_2$ ), quartet  $U@B_{40}^-$  (**2**,  $C_{2v}$ ,  $^4B_1$ ), quintet  $Np@B_{40}^+$  (**3**,  $C_{2v}$ ,  $^5A_1$ ), sextet  $Np@B_{40}$  (**4**,  $C_2$ ,  $^6A$ ), septet  $Pu@B_{40}$  (**5**,  $C_{2v}$ ,  $^7A_2$ ), octet  $Am@B_{40}$  (**6**,  $C_{2v}$ ,  $^8A_2$ ), and octet  $Cm@B_{40}^+$  (**7**,  $C_{2v}$ ,  $^8A_2$ ) at the coupled-cluster with triple excitations CCSD(T) level. Detailed principal interacting spin orbital (PISO) and adaptive natural density partitioning (AdNDP) analyses reveal their coordination bonding patterns and show that, with the numbers of unpaired  $\alpha$ -electrons in parallel spins varying from  $n_\alpha = 2, 3, 4, 5, 6, 7$ , to 7 in these complexes, the percentage contribution of the An 5f-involved PISO pairs to overall coordination bonding interactions decreases monotonously from 41% to 1%, the contribution of An 6d-involved PISO pairs increases monotonously from 47% to 72%, while the marginal contribution of An 7s-involved PISO pairs remains basically unchanged (4~7%). The IR, Raman, and photoelectron spectra of the most concerned species are computationally simulated to facilitate their characterizations in future experiments.

**Keywords:** actinides; Metallo-Borospherenes; first-principles theory; structures; coordination bonding patterns

## 1. Introduction

The discovery of the first all-boron fullerenes  $D_{2d} B_{40}^{0/-}$  in 2014[1] and  $C_3/C_2 B_{39}^-$  in 2015[2] paves the way for borospherene chemistry, with special attention paid to the structures and bonding of metallo-borospherenes.[3] Our group predicted at density functional theory (DFT) level the first endohedral metallo-borospherenes  $C_{2v} Ca@B_{40}$  and  $D_{2d} Sr@B_{40}$  and exohedral metallo-borospherenes  $C_s M@B_{40}$  ( $M = Be, Mg$ ) in 2015.[4] Similar endohedral rare-earth-metal-doped  $C_s Sc@B_{40}$ ,  $C_{2v} Y@B_{40}$ , and  $C_{2v} La@B_{40}$  have also been proposed at DFT.[5] Dong et al. proposed a  $B_{40}$  fullerene decorated with six Ti atoms as a promising candidate for hydrogen storage.[6] Fa et al. studied the structural stability of endohedral  $C_{2v} Na@B_{40}$  and  $D_{2d} Ba@B_{40}$  and exohedral  $C_s M@B_{40}$  ( $M = Li, K$  and  $Tl$ ) at DFT.[7] Sr-doping was found to increase the conductance of  $B_{40}$  fullerene due to the decreased energy gap in  $D_{2d} Sr@B_{40}$ .[8] The Ti atom in  $Ti@B_{40}$  is found to reside very close to the boron framework, while the doubly doped  $Ti_2@B_{40}$  possesses a singlet cube-like structure with  $C_s$  symmetry.[9] The exohedral  $Ni_n@B_{40}$  complex series ( $n = 1-4$ ) feature quasi-planar hepta-coordinate Ni centers on the cage surfaces in  $\eta^7-B_7$  heptagons.[10] Li et al. predicted that Cu, Ag and Au atoms in  $MB_{40}$  ( $M = Cu, Ag$  and  $Au$ ) favor the exohedral configuration.[11] Wang et al. predicted in 2017 the first singlet endohedral actinide-metal-doped  $D_{2d} U@B_{40}$  at the pure DFT Perdew-Burke-Ernzerhof (DFT-PBE) level which, with the U atom located exactly at the center of the  $B_{40}$  cage, satisfies the 32-electron principle of  $1S^2 1P^6 1D^{10} 1F^{14}$ .[12] However, at the hybrid PBE0 level, a slightly distorted triplet  $C_1 U@B_{40}$  appears to be the ground state of the neutral species which lies 0.70 eV more stable than its singlet counterpart

$D_{2d}$   $U@B_{40}$ . [13] Shi et al. systematically explored actinide-doped  $AnB_m$  series ( $An = Ac, Th, Pa, U, Np, Pu, Am, Cm$ ;  $m = 7, 20, 24, 36, 38, 39, 40$ ) and suggested that doping with the right actinides may stabilize  $B_n$  clusters. [14–18] The lanthanide-doped octet  $D_{2d}$   $Eu@B_{40}$  ( $^8B_2$ ) and septet  $C_s$   $Gd@B_{40}$  ( $^7A''$ ) have also been predicted in theory. [19] Li et al. explored the  $ThB_{40}$  which revealed obvious covalent characters between the Th center and the  $B_{40}$  cage. [20]

In this work, we systematically investigated the coordination bonding nature of actinide-doped endohedral borospherenes  $An@B_{40}^{0/+/-}$  ( $An = U, Np, Pu, Am, Cm$ ) at the first-principles theory level. Extensive coupled-cluster calculations with triple excitations (CCSD(T)) reveal the ground states of  $U@B_{40}$  (**1**,  $C_{2v}$ ,  $^3A_2$ ),  $U@B_{40}^-$  (**2**,  $C_{2v}$ ,  $^4B_1$ ),  $Np@B_{40}^{+}$  (**3**,  $C_{2v}$ ,  $^5A_1$ ),  $Np@B_{40}$  (**4**,  $C_2$ ,  $^6A$ ),  $Pu@B_{40}$  (**5**,  $C_{2v}$ ,  $^7A_2$ ),  $Am@B_{40}$  (**6**,  $C_{2v}$ ,  $^8A_2$ ), and  $Cm@B_{40}^{+}$  (**7**,  $C_{2v}$ ,  $^8A_2$ ) with the numbers of unpaired  $\alpha$ -electrons of  $n_\alpha = 2, 3, 4, 5, 6, 7$ , and  $7$ , respectively. Detailed Principal Interacting Spin Orbital (PISO) and adaptive natural density partitioning (AdNDP) analyses unveil the coordination bonding patterns of the complex series and quantitatively evaluated the variation trends of percentage contributions of An 5f-, 6d-, and 7s-involved PISO pairs to the overall coordination bonding energies with the numbers of unpaired  $\alpha$ -electrons ( $n_\alpha$ ) in the complex systems.

## 2. Results and Discussion

### 2.1. Structures and Stabilities

The optimized three lowest-lying isomers with different spin multiplicities of  $U@B_{40}$  and  $U@B_{40}^-$  are shown in Figure 1(a) and Figure 1(b), respectively. The optimized ground-state structures of the  $An@B_{40}^{0/+/-}$  series ( $An = U, Np, Pu, Am, Cm$ ) are collectively shown in Figure 1(c), with their alternative low-lying isomers with different spin multiplicities depicted according to their relative energies in Figure S1. As shown in Figure 1 and Figure S1, the calculated CCSD(T) relative energies at the most accurate theoretical level implemented in this work provide strong evidence to support both the hybrid PBE0 and TPSSh approaches.

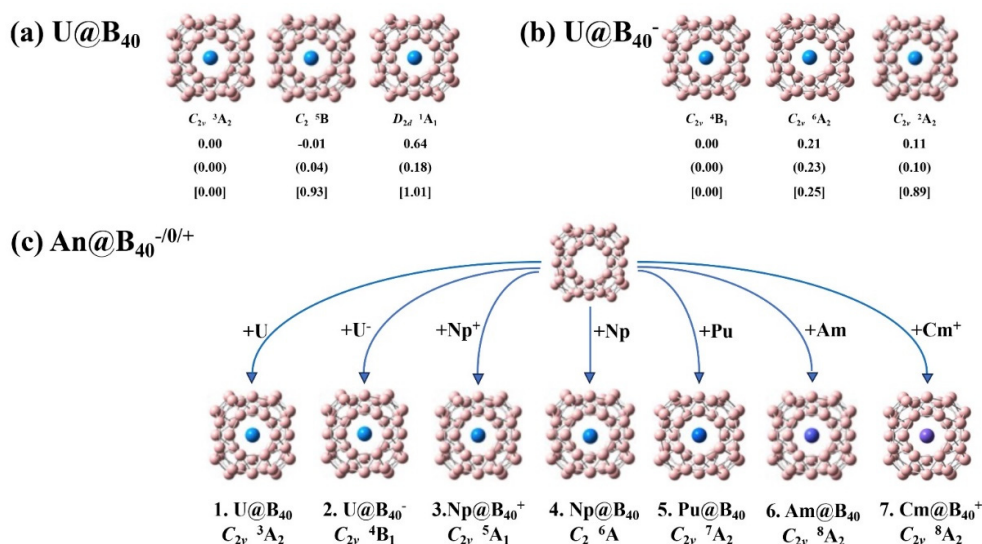


**Figure 1.** Optimized three low-lying isomers of (a)  $U@B_{40}$  and (b)  $U@B_{40}^-$  with their relative energies indicated in eV at PBE0, TPSSh (parentheses), and CCSD(T)/PBE0 (square brackets) levels, respectively, and optimized ground-state structures of (c)  $C_{2v}$   $U@B_{40}$  (**1**,  $^3A_2$ ),  $C_{2v}$   $U@B_{40}^-$  (**2**,  $^4B_1$ ),  $C_{2v}$   $Np@B_{40}^{+}$  (**3**,  $^5A_1$ ),  $C_2$   $Np@B_{40}$  (**4**,  $^6A$ ),  $C_{2v}$   $Pu@B_{40}$  (**5**,  $^7A_2$ ),  $C_{2v}$   $Am@B_{40}$  (**6**,  $^8A_2$ ), and  $C_{2v}$   $Cm@B_{40}^{+}$  (**7**,  $^8A_2$ ) at PBE0.

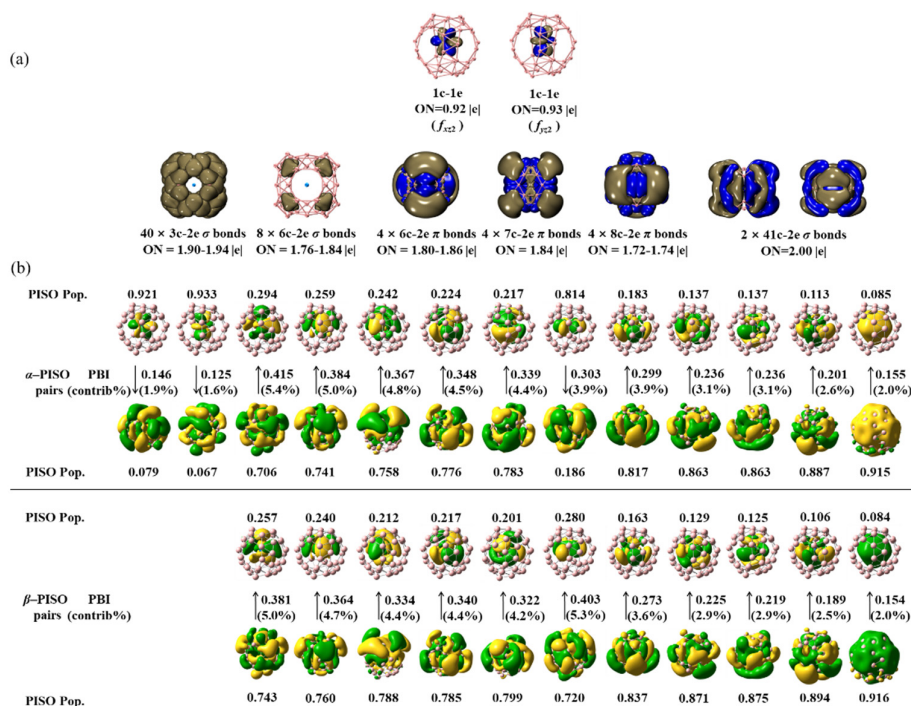
Interestingly, as clearly shown in Figure 1(a), the triplet  $C_{2v}$   $U@B_{40}$  (**1**,  $^3A_2$ ) with two unpaired 5f  $\alpha$ -electrons proves to be the well-defined ground state of the neutral complex which lies 0.93 and 1.01 eV more stable than the quintet  $C_2$   $U@B_{40}$  ( $^5B$ ) and singlet  $D_{2d}$   $U@B_{40}$  ( $^1A_1$ ) at the most accurate CCSD(T)

level achieved in this work, respectively. Such a relative energy order qualitatively agrees with that obtained at both the hybrid DFT-PBE0 and DFT-TPSSH levels, but totally differs from that of previously reported results at pure DFT-PBE.[21] We believe the hybrid DFT and CCSD(T) relative energies are more reliable than that obtained at the pure DFT-PBE. As expected, with one extra electron attached, the  $\text{U@B}_{40}^-$  monoanion with three unpaired 5f  $\alpha$ -electrons appears to have a quartet ground state of  $C_{2v}$   $\text{U@B}_{40}^-$  (**2**,  $^4B_1$ ) which lies 0.25 and 0.89 eV more stable than the sextet  $C_{2v}$   $\text{U@B}_{40}^-$  ( $^6A_2$ ) and doublet  $C_{2v}$   $\text{U@B}_{40}^-$  ( $^2A_2$ ) at CCSD(T), respectively. Detailed BOMD simulations collectively shown in Figure S2 indicate that both  $\text{U@B}_{40}$  (**1**) and  $\text{U@B}_{40}^-$  (**2**) are dynamically stable at 300K, with the small calculated root-mean-square-deviations of RMSD = 0.12, 0.08 Å and maximum bond length deviations of MAXD = 0.41, 27 Å, respectively.

Substituting the U coordination center in  $\text{U@B}_{40}$  (**1**) with heavier actinide metals Np, Pu, Am, and Cm, the quintet  $C_{2v}$   $\text{Np@B}_{40}^+$  (**3**,  $^5A_1$ ), sextet  $C_2$   $\text{Np@B}_{40}$  (**4**,  $^6A$ ), septet  $C_{2v}$   $\text{Pu@B}_{40}$  (**5**,  $^7A_2$ ), octet  $C_{2v}$   $\text{Am@B}_{40}$  (**6**,  $^8A_2$ ), and  $C_{2v}$   $\text{Cm@B}_{40}^+$  (**7**,  $^8A_2$ ) are obtained systematically which prove to be the ground states of the systems, as shown in Figure 1c and Figure S1, with the second lowest-lying  $C_1$   $\text{Np@B}_{40}^+$  ( $^7A$ ),  $C_{2v}$   $\text{Np@B}_{40}$  ( $^4B_2$ ),  $C_{2v}$   $\text{Pu@B}_{40}$  ( $^5B_2$ ),  $C_{2v}$   $\text{Am@B}_{40}$  ( $^{10}B_1$ ), and  $C_s$   $\text{Cm@B}_{40}^+$  ( $^6A'$ ) being 0.41, 0.19, 0.07, 0.04, and 0.77 eV less stable than their corresponding ground states at CCSD(T), respectively. As discussed in details below, the ground states triplet  $\text{U@B}_{40}$  (**1**), quartet  $\text{U@B}_{40}^-$  (**2**), quintet  $\text{Np@B}_{40}^+$  (**3**), sextet  $\text{Np@B}_{40}$  (**4**), septet  $\text{Pu@B}_{40}$  (**5**), octet  $\text{Am@B}_{40}$  (**6**), and octet  $\text{Cm@B}_{40}^+$  (**7**) possess increasing spin multiplicities, with the numbers of unpaired  $\alpha$ -electrons in parallel spins varying from  $n_\alpha = 2, 3, 4, 5, 6, 7$ , to 7, indicating that the increased valence electrons in complexes **1-7** are consecutively distributed in unpaired  $\alpha$ -orbitals of the systems.

## 2.2. Bonding Pattern Analyses

As demonstrations, detailed AdNDP and PISO bonding patterns of the triplet  $C_{2v}$   $\text{U@B}_{40}$  (**1**) are presented in Figure 2. As shown in Figure 2(a),  $\text{U@B}_{40}$  (**1**) contains 1 1c-1e  $f_{xz^2}$ -type bond and 1 1c-1e  $f_{yz^2}$ -type bond on the U coordination center with the occupation numbers of ON = 0.92 and 0.93, respectively, 40 3c-2e and 8 6c-2e  $\sigma$  bonds on the  $\text{B}_{40}$  ligand with ON = 1.76-1.94, 4 6c-2e, 4 7c-2e, and 4 8c-2e  $\pi$  coordination bonds between the  $\text{B}_{40}$  ligand and U center with ON = 1.72-1.86, and 2 41c-2e  $\sigma$  coordination bonds between  $\text{B}_{40}$  and U with ON = 2.00. It is the two unpaired 5f  $\alpha$ -electrons in parallel spins that determine the triplet ground state of the system ( $^3A_2$ ).







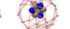




**Figure 2.** (a) AdNDP bonding pattern of triplet  $C_{2v}$   $U@B_{40}$  (**1**), with the occupation numbers (ON) indicated. (b) PISO bonding pattern of  $C_{2v}$   $U@B_{40}$  (**1**) with the U coordination center and  $B_{40}$  ligand as interacting fragments, with the corresponding occupation numbers (PISO Pop.), PIO-based bond indexes (PBI), and percentage contributions (contrib/%) to the overall coordination interactions indicated.

Detailed PISO analyses on  $U@B_{40}$  (**1**) in Figure 2(b) with the  $B_{40}$  ligand and U coordination center as interacting fragments help to unveil a precise description of the coordination bonding pattern in the complex. As clearly shown in Figure 2(b),  $U@B_{40}$  (**1**) has two unpaired  $\alpha$ -PISO 5f orbitals with the PISO populations of 0.921 and 0.933, respectively, as the singly occupied molecular orbitals (SOMOs) of the complex which have no corresponding  $\beta$ -PISO counterparts to correlate with, while all the remaining  $\alpha$ -PISO and  $\beta$ -PISO pairs in exact one-to-one corresponding relationships are fully paired in couples, rendering the system a triplet ground state ( $^3A_2$ ). The two unpaired  $\alpha$ -PISO 5f orbitals turn out to well correspond to the 1c-1e  $f_{xz2}$ -type bond and 1c-1e  $f_{yz2}$ -type bond obtained by AdNDP analyses in Figure 2(a), respectively. Their small PISO-based bond indexes (PBI) of 0.146 and 0.125 indicate that the interactions between the two unpaired  $\alpha$ -PISO U 5f orbitals and the corresponding nearly empty  $\alpha$ -molecular orbitals of  $B_{40}$  ligand with the small PISO populations of 0.079 and 0.067 make marginable contributions (1.9% and 1.6%, respectively) to the overall coordination energy in the complex, with the remaining PISO pairs with PISO 5f populations between 0.084~0.294 and PBI values between 0.154~0.451 dominate the overall coordination interactions between the  $B_{40}$  ligand and U center. In combinations, these PISO pairs result in the 4 6c-2e, 4 7c-2e, and 4 8c-2e  $\pi$  coordination bonds and 2 41c-2e  $\sigma$  coordination bonds obtained in AdNDP analyses discussed above.

As shown in Figure 3, similar AdNDP and PISO bonding patterns exist for quartet  $U@B_{40}^-$  (**2**,  $^4B_1$ ), quintet  $Np@B_{40}^+$  (**3**,  $^5A_1$ ), septet  $Pu@B_{40}$  (**5**,  $^7A_2$ ), octet  $C_{2v}$   $Am@B_{40}$  (**6**,  $^8A_2$ ), and octet  $C_{2v}$   $Cm@B_{40}^+$  (**7**,  $^8A_2$ ) which possess three, four, six, seven, and seven unpaired  $\alpha$ -PISO 5f electrons with the PISO populations between 0.87~0.91, 0.93~0.99, 0.79~0.98, 0.91~0.99, and 0.99~1.00 and PISO-based bond indexes between PBI = 0.16~0.23, 0.03~0.12, 0.04~0.34, 0.01~0.17, 0.01~0.02, respectively. Interestingly, the  $\alpha$ -SOMO of the sextet  $Np@B_{40}$  (**4**) which contributes 7.8% to the overall coordination interaction turns out to be a typical  $\alpha$ -bond with the comparable Np 5f  $\alpha$ -PISO population of 0.432 and  $B_{40}$   $\beta$ -PISO population of 0.568 and the PISO-based bond index of PBI = 0.491, respectively. Such an  $\alpha$ -bond with nonnegligible contributions from both the Np coordination center and  $B_{40}$  ligand corresponds to a 41c-1e bond in AdNDP bonding analyses, as clearly shown in Figure 3.

structure	U <sub>B<sub>40</sub></sub>		U <sub>B<sub>40</sub></sub> <sup>−</sup>		NpB <sub>40</sub> <sup>+</sup>		NpB <sub>40</sub>		PuB <sub>40</sub>	
electronic state	<sup>3</sup> A <sub>2</sub>		<sup>4</sup> B <sub>1</sub>		<sup>5</sup> A <sub>1</sub>		<sup>6</sup> A		<sup>7</sup> A <sub>1</sub>	
unpaired 5f electrons	2		3		4		5		6	
PISO analysis	PISO Pop.	0.921 0.933	0.867 0.877 0.913	0.934 0.949 0.982 0.987	0.432 0.945 0.954 0.999 0.960	0.786 0.916 0.946 0.964 0.967 0.981				
	PBI (contrib%)	0.146 0.125 (1.9%) (1.6%)	0.231 0.216 0.159 (2.8%) (2.5%) (1.9%)	0.122 0.097 0.035 0.026 (1.9%) (1.5%) (0.5%) (0.4%)	0.491 0.104 0.087 0.079 0.077 (7.8%) (1.7%) (1.4%) (1.3%) (1.2%)	0.336 0.154 0.102 0.069 0.063 0.030 (6.4%) (2.9%) (1.9%) (1.3%) (1.2%) (0.7%)				
	PISO Pop.	0.079 0.067	0.133 0.123 0.087	0.066 0.051 0.018 0.013	0.568 0.055 0.046 0.041 0.040	0.214 0.084 0.054 0.036 0.033 0.015				
The corresponding AdNDP bonds										
	1c-1e ON=0.921c ON=0.933e		1c-1e ON=0.877c ON=0.883e ON=0.913e		1c-1e ON=0.949c ON=0.955e ON=0.982c ON=0.987e		41c-1e ON=1.001c ON=0.955e ON=0.955e ON=0.962c ON=0.962e		1c-1e ON=0.792c ON=0.946c ON=0.962c ON=0.972c ON=0.972c ON=0.972c	
structure	AmB <sub>40</sub>		CmB <sub>40</sub> <sup>+</sup>							
electronic state	<sup>8</sup> A <sub>2</sub>		<sup>8</sup> A <sub>2</sub>							
unpaired 5f electrons	7		7							
PISO analysis	PISO Pop.	0.907 0.920 0.949 0.963 0.964 0.982 0.993	0.992 0.992 0.994 0.995 0.996 0.996 0.997							
	PBI (contrib%)	0.168 0.146 0.097 0.072 0.069 0.035 0.013 (4.0%) (3.6%) (2.7%) (1.9%) (1.8%) (0.9%) (0.3%)	0.016 0.015 0.011 0.010 0.009 0.008 0.006 (0.37%) (0.31%) (0.21%) (0.20%) (0.19%) (0.18%) (0.15%)							
	PISO Pop.	0.093 0.080 0.051 0.037 0.036 0.018 0.007	0.008 0.008 0.006 0.005 0.004 0.004 0.003							
The corresponding AdNDP bonds										
	1c-1e ON=0.921c ON=0.921e ON=0.949c ON=0.977e ON=0.977e ON=0.982c ON=0.993e		1c-1e ON=0.992c ON=0.992e ON=0.994c ON=0.995e ON=0.996c ON=0.996e ON=0.997e							

**Figure 3.** Unpaired PISO  $\alpha$ -orbitals of  $U@B_{40}$  (**1**,  $^3A_2$ ),  $U@B_{40}^-$  (**2**,  $^4B_1$ ),  $Np@B_{40}^+$  (**3**,  $^5A_1$ ),  $Np@B_{40}$  (**4**,  $^6A$ ),  $Pu@B_{40}$  (**5**,  $^7A_2$ ),  $Am@B_{40}$  (**6**,  $^8A_2$ ), and  $Cm@B_{40}^+$  (**7**,  $^8A_2$ ), with the  $\alpha$ -spin occupation numbers (PISO Pop.) associated with the principal interacting spin orbitals, PISO-based bond indexes (PBI), and their percentage contributions (contrib/%) to the overall coordination interactions between the An

coordination center and B<sub>40</sub> ligand indicated. The corresponding AdNDP analyses of the singly occupied 1c-1e  $\alpha$ -5f orbitals in **1**, **2**, **3**, **5**, **6**, and **7** and 41c-1e  $\alpha$ -bond in Np@B<sub>40</sub> (**4**) are compared at the bottom, with the occupation numbers (ON) indicated.

### 2.3. Percentage Contributions of An 5f-, 6d-, and 7s-Involved PISO Pairs to the Overall Coordination Interactions

To compare the percentage contributions of An 5f-, 6d-, and 7s-involved PISO pairs to the overall An--B<sub>40</sub> coordination interaction energies, we categorized the orbital types of An atoms involved in the PISO bonding patterns by their orbital shapes and consider the contributions of the corresponding PISO pairs separately. As shown in Figure 4, with the numbers of unpaired  $\alpha$ -electrons in parallel spins varying from  $n_\alpha = 2, 3, 4, 5, 6, 7$ , to 7 in the complex series, the calculated overall An--B<sub>40</sub> coordination interaction energies decrease generally from U@B<sub>40</sub> (**1**, <sup>3</sup>A<sub>2</sub>), U@B<sub>40</sub><sup>-</sup> (**2**, <sup>4</sup>B<sub>1</sub>), Np@B<sub>40</sub><sup>+</sup> (**3**, <sup>5</sup>A<sub>1</sub>), Np@B<sub>40</sub> (**4**, <sup>6</sup>A), Pu@B<sub>40</sub> (**5**, <sup>7</sup>A<sub>2</sub>), to Am@B<sub>40</sub> (**6**, <sup>8</sup>A<sub>2</sub>) and increase slightly at Cm@B<sub>40</sub><sup>+</sup> (**7**, <sup>8</sup>A<sub>2</sub>), with the percentage contributions of An 5f-involved PISO pairs to the overall coordination bonding interactions decreasing monotonously from 41% to 1%, the dominating contributions of An 6d-involved PISO pairs increasing monotonously from 47% to 72%, and the marginal contributions of An 7s-involved PISO pairs remaining basically unchanged (4~7%). The slight increase in overall coordination interaction energy at Cm@B<sub>40</sub><sup>+</sup> (**7**) mainly originates from the obvious increased contribution of the Cm 6d orbitals. These results show that with the metal center varying from U, Np, Pu, Am, to Cm, the tendency of the An-5f orbitals to participate in coordination bonding interactions with the B<sub>40</sub> ligand weakens gradually from left to right in the periodic table, with the seven unpaired 5f  $\alpha$ -electrons (5f<sup>7</sup>) in Cm@B<sub>40</sub><sup>+</sup> (**7**) contribute only about 1% to the overall coordination interaction energy, indicating an obvious actinide contraction in atomic radii from left to right in the periodic table. Figure 4 indicates that the An 6d atomic orbitals dominate the coordination interaction between the An centers and B<sub>40</sub> ligand in the concerned An@B<sub>40</sub> species, while An 5f and 7s make only minor contributions.

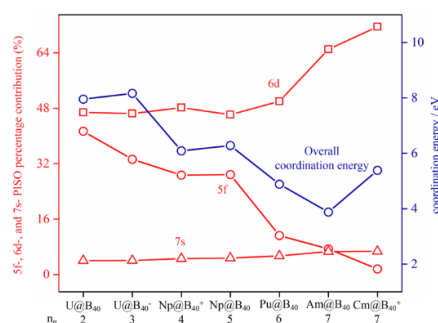
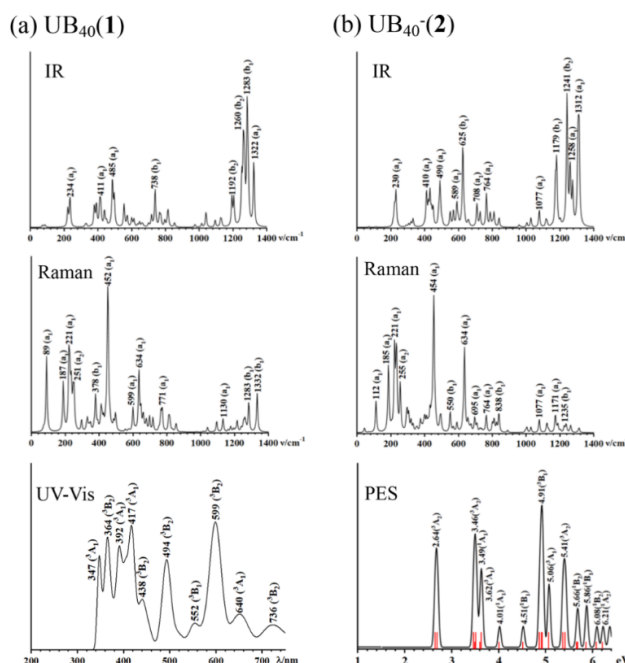


**Figure 4.** Variation of the calculated overall An--B<sub>40</sub> coordination interaction energies highlighted in blue and the corresponding PISO percentage contributions of 5f-, 6d-, and 7s-orbital-involved pair interactions highlighted in red in U@B<sub>40</sub> (**1**, <sup>3</sup>A<sub>2</sub>), U@B<sub>40</sub><sup>-</sup> (**2**, <sup>4</sup>B<sub>1</sub>), Np@B<sub>40</sub><sup>+</sup> (**3**, <sup>5</sup>A<sub>1</sub>), Np@B<sub>40</sub> (**4**, <sup>6</sup>A), Pu@B<sub>40</sub> (**5**, <sup>7</sup>A<sub>2</sub>), Am@B<sub>40</sub> (**6**, <sup>8</sup>A<sub>2</sub>), and Cm@B<sub>40</sub><sup>+</sup> (**7**, <sup>8</sup>A<sub>2</sub>) with the numbers of singly occupied 5f electrons ( $n_\alpha$ ) at PBE0 level.

### 2.4. Simulated IR, Raman and PE Spectra

Infrared (IR) and photoelectron spectra (PES) measurements have proven to be the powerful approaches to characterize boron nanoclusters in gas phases.[1–3] We depict the simulated IR, Raman, and UV-Vis spectra of U@B<sub>40</sub> (**1**) in Figure 5(a) and the calculated IR, Raman, and PES of U@B<sub>40</sub><sup>-</sup> (**2**) in Figure 5(b) at PBE0 level to facilitate their future experimental characterizations. U@B<sub>40</sub> (**1**) exhibits strong IR peaks at 234 (a<sub>1</sub>), 411 (a<sub>1</sub>), 485 (a<sub>1</sub>), 738 (b<sub>1</sub>), and 1283 (b<sub>1</sub>) cm<sup>-1</sup>, while its Raman spectrum features strong vibrational modes at 89 (a<sub>1</sub>), 221 (a<sub>1</sub>), 452 (a<sub>1</sub>), 634 (a<sub>1</sub>), and 1332 (b<sub>1</sub>). It is noticed that U@B<sub>40</sub> (**1**) and U@B<sub>40</sub><sup>-</sup> (**2**) possess the radial breathing modes (RBMs) at 452 cm<sup>-1</sup> (a<sub>1</sub>) and

454  $\text{cm}^{-1}$  ( $a_1$ ), respectively, which turns out to be slightly blue-shifted from that (428  $\text{cm}^{-1}$  ( $a_1$ )) of the empty  $D_{2d}$  B<sub>40</sub> borospherene at the same theoretical level. Similar IR and Raman spectra exist for  $\text{U@B}_{40}^-$  (**2**). The UV-vis spectrum of  $\text{U@B}_{40}$  (**1**) and PES spectrum of  $\text{U@B}_{40}^-$  (**2**) were calculated using the time-dependent DFT approach (TD-DFT) at PBE0 level. Since  $\text{U@B}_{40}^-$  has a quartet state, one-electron detachment from the anion could lead to triplet or singlet final states in the neutral. The first vertical detachment energy at  $\text{VDE1} = 2.64$  eV ( $^3A_2$ ) for  $\text{U@B}_{40}^-$  was calculated as the energy difference between the anionic ground state and the neutral ground state at the optimized anion geometry. Higher vertical detachment energies at  $\text{VDE} = 3.46$  ( $^3B_1$ ), 4.91 ( $^3B_1$ ), and 5.41 ( $^3A_2$ ) eV correspond to vertical detachment transitions to the excited states of the neutral.



Chemical bonding patterns were analyzed employing both the AdNDP [34,35] method and principal interacting orbital (PIO) [36] approach based on the natural population analyses using the NBO 6.0[37] program. In this work, PISO [38] analyses based on PIO calculations were performed on the open-shell  $An@B_{40}^{0/+}$  series. The PIO analyses were also carried out using the Gaussian 09 program with 6-31G\* basis set used for B atoms and ECP60MWB\_SEG employed for An. The VMD[39] program was used for the visualization of structures and molecular orbitals.

## 5. Conclusions

In summary, we have predicted in this work the ground states of triplet  $U@B_{40}$  (1), quartet  $U@B_{40}^-$  (2), quintet  $Np@B_{40}^+$  (3), sextet  $Np@B_{40}$  (4), septet  $Pu@B_{40}$  (5), octet  $Am@B_{40}$  (6), and octet  $Cm@B_{40}^+$  (7) at CCSD(T) level, revealed their coordination bonding patterns using both the PISO and AdNDP approaches, and calculated the percentage contributions of An 5f-, 6d-, and 7s-involved PISO pairs to the overall coordination interaction energies at PBE0 level, respectively, unveiling the coordination bonding nature of these actinide-doped endohedral metallo-borospherenes both qualitatively and quantitatively. Such high spin-multiplicity actinide-doped endohedral metallo-borospherenes could be expanded to all the actinides in the periodic table to form various magnetic complexes and crystals with potential applications in digital device.

**Supplementary Materials:** The following supporting information can be downloaded at the website of this paper posted on Preprints.org, Figure S1: Relative energies of the low-lying isomers of  $An@B_{40}^{0/+}$  (An = Np to Cm) with different spin multiplicities at PBE0/B/6-311+G\*/An/ECP60MWB, TPSSH/B/6-311+G\*/An/ECP60MWB, and CCSD(T) levels, Figure S2: Molecular dynamics simulations of  $U@B_{40}$  (1) and  $U@B_{40}^-$  (2) at 300 K, with the calculated root-mean-square-deviations (RMSD) and maximum bond length deviations (MAXD) indicated, respectively, Table S1: Optimized coordinates (x, y, z) of  $C_{2v}$   $U@B_{40}$  (1),  $C_{2v}$   $U@B_{40}^-$  (2),  $C_{2v}$   $Np@B_{40}^+$  (3),  $C_2$   $Np@B_{40}$  (4),  $C_{2v}$   $Pu@B_{40}$  (5),  $C_{2v}$   $Am@B_{40}$  (6) and  $C_{2v}$   $Cm@B_{40}^+$  (7) at PBE0 level.

**Author Contributions:** S.L. conceived the project and finalized the manuscript. X.Z. performed the DFT calculations. Z.W. and S.L. provided valuable discussion. X.Z wrote the manuscript, and all authors participated in the revision of the manuscript and agreed to the published version of the manuscript.

**Data Availability Statement:** All the data are available online.

**Acknowledgments:** The work was supported by the National Natural Science Foundation of China (22373061 and 21973057 to S.-D. Li).

**Conflicts of Interest:** The authors declare no conflicts of interest.

## References

1. Zhai, H.J.; Zhao, Y.F.; Li, W.L.; Chen, Q.; Bai, H.; Hu, H.S.; Piazza, Z.A.; Tian, W.J.; Lu, H.G.; Wu, Y.B.; et al. Observation of an All-Boron Fullerene. *Nat Chem* **2014**, *6*, 727–731, doi:10.1038/nchem.1999.
2. Chen, Q.; Li, W.L.; Zhao, Y.F.; Zhang, S.Y.; Hu, H.S.; Bai, H.; Li, H.R.; Tian, W.J.; Lu, H.G.; Zhai, H.J.; et al. Experimental and Theoretical Evidence of an Axially Chiral Borospherene. *ACS Nano* **2015**, *9*, 754–760, doi:10.1021/nn506262c.
3. Jian, T.; Chen, X.; Li, S.D.; Boldyrev, A.I.; Li, J.; Wang, L.S. Probing the Structures and Bonding of Size-Selected Boron and Doped-Boron Clusters. *Chem Soc Rev* **2019**, *48*, 3550–3591, doi:10.1039/c9cs00233b.
4. Bai, H.; Chen, Q.; Zhai, H.J.; Li, S.D. Endohedral and Exohedral Metalloborospherenes:  $M@B_{40}$  (M = Ca, Sr) and  $M\&B_{40}$  (M = Be, Mg). *Angewandte Chemie—International Edition* **2015**, *54*, 941–945, doi:10.1002/anie.201408738.
5. Jin, P.; Hou, Q.; Tang, C.; Chen, Z. Computational Investigation on the Endohedral Borofullerenes  $M@B_{40}$  (M = Sc, Y, La). *Theor Chem Acc* **2015**, *134*, 1–10, doi:10.1007/s00214-014-1612-4.
6. Dong, H.; Hou, T.; Lee, S.T.; Li, Y. New Ti-Decorated B 40 Fullerene as a Promising Hydrogen Storage Material. *Sci Rep* **2015**, *5*, 1–8, doi:10.1038/srep09952.
7. Fa, W.; Chen, S.; Pande, S.; Zeng, X.C. Stability of Metal-Encapsulating Boron Fullerene  $B_{40}$ . *Journal of Physical Chemistry A* **2015**, *119*, 11208–11214, doi:10.1021/acs.jpca.5b07173.
8. An, Y.; Zhang, M.; Wu, D.; Fu, Z.; Wang, T.; Xia, C. Electronic Transport Properties of the First All-Boron Fullerene  $B_{40}$  and Its Metallofullerene  $Sr@B_{40}$ . *Physical Chemistry Chemical Physics* **2016**, *18*, 12024–12028, doi:10.1039/c6cp01096b.
9. Jin, P.; Yang, L.; Liu, C.; Hou, Q.; Li, L. Computational Prediction of the Endohedral Metalloborofullerenes  $Tin@B_{40}$  (n = 1, 2). *Theor Chem Acc* **2017**, *136*, 1–12, doi:10.1007/s00214-017-2087-x.



10. Li, H.R.; Tian, X.X.; Luo, X.M.; Yan, M.; Mu, Y.W.; Lu, H.G.; Li, S.D. Heteroborospherene Clusters  $Ni_n B_{40}$  ( $n = 1-4$ ) and Heteroborophene Monolayers  $Ni_2 B_{14}$  with Planar Heptacoordinate Transition-Metal Centers in  $H7-B7$  Heptagons. *Sci Rep* **2017**, *7*, 1–7, doi:10.1038/s41598-017-06039-9.
11. Li, S.X.; Zhang, Z.P.; Long, Z.W.; Qin, S.J. Structures, Stabilities and Spectral Properties of Metalloborospherenes  $MB_0/40$  ( $M = Cu, Ag, \text{ and } Au$ ). *RSC Adv* **2017**, *7*, 38526–38537, doi:10.1039/c7ra05932a.
12. Yu, T.; Gao, Y.; Xu, D.; Wang, Z. Actinide Endohedral Boron Clusters: A Closed-Shell Electronic Structure of  $U@B_{40}$ . *Nano Res* **2018**, *11*, 354–359, doi:10.1007/s12274-017-1637-9.
13. Wang, J.; Xie, W.; Jiang, W.; Wu, X.; Wang, Z. The Reliability of the Density-Functional Theory in Actinide Endohedral Systems. *Adv Theory Simul* **2019**, *2*, 1–7, doi:10.1002/adts.201900138.
14. Zhang, N.; Li, A.; Wang, C.; Wu, Q.; Lan, J.; Chai, Z.; Zhao, Y.; Shi, W. Theoretical Prediction of Chiral Actinide Endohedral Borospherenes. *New Journal of Chemistry* **2021**, *45*, 6803–6810, doi:10.1039/d1nj00211b.
15. Zhang, N.; Wang, C.; Wu, Q.; Lan, J.; Chai, Z.; Shi, W. Highly Stable Actinide(III) Complexes Supported by Doubly Aromatic Ligands†. *Physical Chemistry Chemical Physics* **2022**, *24*, 5921–5928, doi:10.1039/d1cp05058c.
16. Wang, C.Z.; Bo, T.; Lan, J.H.; Wu, Q.Y.; Chai, Z.F.; Gibson, J.K.; Shi, W.Q. Ultrastable Actinide Endohedral Borospherenes. *Chemical Communications* **2018**, *54*, 2248–2251, doi:10.1039/c7cc09837e.
17. Wang, J.; Wang, C.Z.; Wu, Q.Y.; Lan, J.H.; Chai, Z.F.; Nie, C.M.; Shi, W.Q. Construction of the Largest Metal-Centered Double-Ring Tubular Boron Clusters Based on Actinide Metal Doping. *Journal of Physical Chemistry A* **2022**, *126*, 3445–3451, doi:10.1021/acs.jpca.2c00563.
18. Zhang, N.; Wang, C.; Wu, Q.; Lan, J.; Chai, Z.; Shi, W. Highly Stable Actinide(III) Complexes Supported by Doubly Aromatic Ligands†. *Physical Chemistry Chemical Physics* **2022**, *24*, 5921–5928, doi:10.1039/d1cp05058c.
19. Xi, C.; Yang, L.; Liu, C.; You, P.; Li, L.; Jin, P. Lanthanide Metals in the Boron Cages: Computational Prediction of  $M@B_n$  ( $M = Eu, Gd; n = 38, 40$ ). *Int J Quantum Chem* **2018**, *118*, 1–11, doi:10.1002/qua.25576.
20. Li, Y.; Wang, Y.; Zhou, Z.; Gao, Y.; Chen, Y.; Zhang, G.; Ma, C. Insights into  $ThB_{40}$ : Stability, Electronic Structure, and Interaction. *Molecules* **2024**, *29*, doi:10.3390/molecules29061222.
21. Wang, J.; Xie, W.; Jiang, W.; Wu, X.; Wang, Z. The Reliability of the Density-Functional Theory in Actinide Endohedral Systems. *Adv Theory Simul* **2019**, *2*, 1–7, doi:10.1002/adts.201900138.
22. Adamo, C.; Barone, V. Toward Reliable Density Functional Methods without Adjustable Parameters: The PBE0 Model. *Journal of Chemical Physics* **1999**, *110*, 6158–6170, doi:10.1063/1.478522.
23. Staroverov, V.N.; Scuseria, G.E.; Tao, J.; Perdew, J.P. Comparative Assessment of a New Nonempirical Density Functional: Molecules and Hydrogen-Bonded Complexes. *Journal of Chemical Physics* **2003**, *119*, 12129–12137, doi:10.1063/1.1626543.
24. Krishnan, R.; Binkley, J.S.; Seeger, R.; Pople, J.A. Self-Consistent Molecular Orbital Methods. XX. A Basis Set for Correlated Wave Functions. *J Chem Phys* **1980**, *72*, 650–654, doi:10.1063/1.438955.
25. Cao, X.; Dolg, M. Segmented Contraction Scheme for Small-Core Actinide Pseudopotential Basis Sets. *Journal of Molecular Structure: THEOCHEM* **2004**, *673*, 203–209, doi:10.1016/j.theochem.2003.12.015.
26. Cao, X.; Dolg, M.; Stoll, H. Valence Basis Sets for Relativistic Energy-Consistent Small-Core Actinide Pseudopotentials. *Journal of Chemical Physics* **2003**, *118*, 487–496, doi:10.1063/1.1521431.
27. Guo, Y.; Riplinger, C.; Becker, U.; Liakos, D.G.; Minenkov, Y.; Cavallo, L.; Neese, F. Communication: An Improved Linear Scaling Perturbative Triples Correction for the Domain Based Local Pair-Natural Orbital Based Singles and Doubles Coupled Cluster Method [DLPNO-CCSD(T)]. *Journal of Chemical Physics* **2018**, *148*, doi:10.1063/1.5011798.
28. Neese, F. The ORCA Program System. *Wiley Interdiscip Rev Comput Mol Sci* **2012**, *2*, 73–78, doi:10.1002/wcms.81.
29. Pantazis, D.A.; Neese, F. All-Electron Scalar Relativistic Basis Sets for the Actinides. *J Chem Theory Comput* **2011**, *7*, 677–684, doi:10.1021/ct100736b.
30. Frisch, M.J.; Trucks, G.W.; Schlegel, H.B.; Scuseria, G.; Robb, M.; Cheeseman, J.; Scalmani, G.; Barone, V.; Mennucci, B.; Petersson, G.; et al. Gaussian 09, Revision D.01, Gaussian, Inc.: Wallingford, CT, USA, 2013.
31. Vandevondele, J.; Krack, M.; Mohamed, F.; Parrinello, M.; Chassaing, T.; Hutter, J. Quickstep: Fast and Accurate Density Functional Calculations Using a Mixed Gaussian and Plane Waves Approach. *Comput Phys Commun* **2005**, *167*, 103–128, doi:10.1016/j.cpc.2004.12.014.
32. Bauernschmitt, R.; Ahlrichs, R. Treatment of Electronic Excitations within the Adiabatic Approximation of Time Dependent Density Functional Theory. *Chem Phys Lett* **1996**, *256*, 454–464, doi:10.1016/0009-2614(96)00440-X.
33. Casida, M.E.; Jamorski, C.; Casida, K.C.; Salahub, D.R. Molecular Excitation Energies to High-Lying Bound States from Time-Dependent Density-Functional Response Theory: Characterization and Correction of the Time-Dependent Local Density Approximation Ionization Threshold. *Journal of Chemical Physics* **1998**, *108*, 4439–4449, doi:10.1063/1.475855.

34. Zubarev, D.Y.; Boldyrev, A.I. Developing Paradigms of Chemical Bonding: Adaptive Natural Density Partitioning. *Physical Chemistry Chemical Physics* **2008**, *10*, 5207–5217, doi:10.1039/b804083d.
35. Tkachenko, N. V.; Boldyrev, A.I. Chemical Bonding Analysis of Excited States Using the Adaptive Natural Density Partitioning Method. *Physical Chemistry Chemical Physics* **2019**, *21*, 9590–9596, doi:10.1039/c9cp00379g.
36. Zhang, J.X.; Sheong, F.K.; Lin, Z. Unravelling Chemical Interactions with Principal Interacting Orbital Analysis. *Chemistry—A European Journal* **2018**, *24*, 9639–9650, doi:10.1002/chem.201801220.
37. Glendening, E.D.; Landis, C.R.; Weinhold, F. NBO 6.0: Natural Bond Orbital Analysis Program. *J Comput Chem* **2013**, *34*, 1429–1437, doi:10.1002/jcc.23266.
38. Sheong, F.K.; Zhang, J.X.; Lin, Z. Principal Interacting Spin Orbital: Understanding the Fragment Interactions in Open-Shell Systems. *Physical Chemistry Chemical Physics* **2020**, *22*, 10076–10086, doi:10.1039/d0cp00127a.
39. Humphrey, W.; Dalke, A.; Schulten, K. VMD: Visual Molecular Dynamics. *J Mol Graph* **1996**, *14*, 33–38, doi:https://doi.org/10.1016/0263-7855(96)00018-5.

**Disclaimer/Publisher's Note:** The statements, opinions and data contained in all publications are solely those of the individual author(s) and contributor(s) and not of MDPI and/or the editor(s). MDPI and/or the editor(s) disclaim responsibility for any injury to people or property resulting from any ideas, methods, instructions or products referred to in the content.